Impact of Head Rotation on the Individualized Common Carotid Flow and Carotid Bifurcation Hemodynamics

Nicolas Aristokleous, Ioannis Seimenis, Georgios C. Georgiou, Yannis Papaharilaou, Brigitta C. Brott, Andrew Nicolaides, and Andreas S. Anayiotos

***Abstract*—This paper aims at evaluating the changes that head rotation poses on morphological and flow characteristics of the carotid bifurcation (CB) and on the distribution of parameters that are regarded as important in atherosclerosis development, such as relative particle residence time (RRT), normalized oscillatory shear index (nOSI), and helicity (HL). Using a subject-specific approach, six healthy volunteers were MR-scanned in two head postures: supine neutral and prone with rightward head rotation. Cross-sectional flow velocity distribution was obtained using phase-contrast MRI at the common carotid artery (CCA). Our results indicate that peak systolic flow rate is reduced at the prone position in most cases for both CCAs. Morphological MR images are used to segment and construct the CB models. Numerical simulations are performed and areas exposed to high helicity or unfavorable hemodynamics are calculated. Head rotation affects the instantaneous spatial extent of high helicity regions. Posture-related observed differences in the distribution of nOSI and RRT suggest that inlet flow waveform tends to moderate geometry-induced changes in the qualitative and quantitative distribution of atherosclerosis-susceptible wall regions. Overall, presented results indicate that an individualized approach is required to fully assess the postural role in atherosclerosis development and in complications arising in stenotic and stented vessels.**

***Index Terms*—Atherosclerosis, carotid artery bifurcation, imaged-based computational fluid dynamics (CFD), wall shear stress.**

I. Introduction

CARDIOVASCULAR disease (CVD) causes over 800 thousand deaths in the United States (US) and 1.9 million in the European Union (EU) per year, amounting to 32% and 40% of all deaths, respectively [1], [2]. Additionally, stroke accounted for around 137 thousand deaths in US and 460 thousand in EU in 2012. To approach the atherosclerosis disease from the personalized medicine point of view, novel markers associated with gene factors, environmental factors, and gene-by-environment interactions must be validated [3]. This paper falls within the general scope of assessing the ability of various hemodynamic markers, related to flow conditions in the carotid, to provide a subject-specific estimation of the geometry-dependent hemodynamic burden on the carotid wall.

Previous studies employing rigid and compliant models regard arterial bifurcations and curvature regions as regions of low and oscillating wall shear stress (WSS) [4]–[10]. For that reason, many researchers have suggested the use of a variety of hemodynamic parameters, such as WSS, WSS temporal gradient (WSSTG), WSS spatial gradient (WSSSG), oscillatory shear index (OSI), normalized OSI (nOSI), and relative residence time (RRT), as potential markers to quantify the blood flow disturbance and indicate possible regions prone to atherogenesis [11]–[13]. Additionally, many geometric parameters, or relevant independent factors [14], have been proposed for describing the arterial geometry. This study focuses on the assessment of the impact that geometry poses on the local hemodynamics using accurate subject-specific models and inlet waveforms. Our approach is based on the accurate reconstruction of the arterial geometry using morphological data acquired from magnetic resonance imaging (MRI) and on velocity measurements obtained with phase-contrast MRI (PC-MRI). To accurately estimate the subject-specific hemodynamic environment *in vivo*, an image-based computational fluid dynamics (CFD) approach is necessary. Steinman and Taylor reviewed the progress achieved in the field of image-based CFD studies in the last decade [14], [15]. The methodology employed in the present work, from MR images to numerical simulations, has been widely applied [15]–[19]. The combination of MRI with CFD allows for more accurate and highly reproducible results, as recently shown by Bijari *et al.* [20] and earlier by other researchers [16], [21]–[25]. Our previous studies in the healthy carotid bifurcation (CB) focused on geometric changes due to head rotation [26], and alterations of the hemodynamic features as a result of that geometry change [27]. The present study aims to evaluate, on a subject-specific basis, the effect of head and neck rotation on: 1) the blood flow waveform and total flow through the common carotid; 2) the local hemodynamics

Manuscript received April 30, 2013; revised December 30, 2013; accepted February 1, 2014. Date of publication February 20, 2014; date of current version May 1, 2014. This work was co-funded by the European Regional Development Fund and the Republic of Cyprus through the Research Promotion Foundation (Project ΥΓΕΙΑ/ΔΥΓΕΙΑ/0609(BIE)/11).

N. Aristokleous and A. S. Anayiotos are with the Department of Mechanical Engineering and Materials Science and Engineering, Cyprus University of Technology, Limassol 3036, Cyprus (e-mail: n.aristokleous@cut.ac.cy; andreas.anayiotos@cut.ac.cy)

I. Seimenis is with the Department of Medical School, Democritus University of Thrace, Alexandroupolis, 68100, Greece (e-mail: iseimen@med.duth.gr).

G. C. Georgiou is with the Department of Mathematics and Statistics, University of Cyprus, Nicosia 1678, Cyprus (e-mail: georgios@ucy.ac.cy).

Y. Papaharilaou is with IACM FORTH, Heraklion 70013, Greece (e-mail: yannisp@iacm.forth.gr).

B. C. Brott is with the Department of Medicine, University of Alabama at Birmingham, Birmingham, AL 35233 USA (e-mail: bbrott@uab.edu).

A. Nicolaides is with the Vascular Screening and Diagnostic Center, Nicosia 70013, Cyprus (e-mail: anicolaides1@gmail.com).

Color versions of one or more of the figures in this paper are available online at http://ieeexplore.ieee.org.

Digital Object Identifier 10.1109/JBHI.2014.2305575

2168-2194 © 2014 IEEE. Personal use is permitted, but republication/redistribution requires IEEE permission.
See http://www.ieee.org/publications_standards/publications/rights/index.html for more information.

combining the resulting arterial geometry changes with various inlet boundary conditions; and 3) the regional distribution of atherosclerotic burden.

II. Materials and Methods

A. Study Group

Six asymptomatic, presumably healthy male volunteers (mean age of 30 years, range from 22 to 39 years) were MR-scanned to obtain the three-dimensional (3-D) arterial models, as well as the total velocity time history through the vessel cross section, of both common carotid arteries (CCAs). Each subject was imaged in two different scanning sessions corresponding to the two investigated head postures: 1) the supine neutral head position (S) and 2) the prone position with rightwards head rotation up to 80° (P). The study was approved by the Cyprus bioethics committee (2011).

B. MR Imaging

All MRI data were acquired with a 3T system (Achieva, Philips Medical Systems, Best, The Netherlands) using the built-in quadrature body coil for proton excitation. A phased array head-neck coil and a phased array superficial coil were used for signal detection in the supine and prone position, respectively. Anatomical data were obtained with a 3-D time-of-flight (TOF) method. For each head posture, careful planning allowed for the complete coverage of both the left and right CBs by including parts of the CCA, the internal carotid artery (ICA) and the external carotid artery (ECA). As a result, four arterial models were obtained per volunteer: supine position left carotid (SPLC), supine position right carotid (SPRC), prone position left carotid (PPLC) and prone position right carotid (PPRC). The employed gradient-echo pulse sequence (echo time (TE) = 3.5 ms, repetition time (TR) = 23 ms, flip angle (FA) = 20°, $0.36 \times 0.36 \times 1.2$ mm^3 acquisition voxel) provided 100 axial, overlapping (by 50%) slices with a reconstruction voxel of $0.2 \times 0.2 \times 0.6$ mm^3. Variable FA and gradient first moment nulling techniques were employed to decrease saturation effects of inflowing blood and reduce signal loss due to complex flow, respectively. A peripheral pulse-triggered, two-dimensional (2-D), phase-sensitive pulse sequence was employed to acquire flow data spread in 20 phases over the cardiac cycle. The gradient echo sequence employed (TE = 13 ms, TR = 20 ms, FA = 10°, $0.35 \times 0.35 \times 5.0$ mm^3 acquisition/reconstruction voxel) provided magnitude and phase-difference, velocity-encoded images using a view sharing reconstruction. An independent scan was prescribed for each CCA in both head positions to ensure that the measurement slice was always perpendicular to the flowing blood and at the level of approximately 3 diameters (∼20 mm) below CB. Optimum encoding velocity per scan was decided upon trial runs.

C. Surface Reconstruction

The 3-D surface models were constructed from the acquired anatomical MR images using slice-by-slice manual segmentation performed with the ITK-Snap (PICSL, USA) software [28]. The vascular modeling toolkit (VMTK) was used for 3-D surface smoothing and to add cylindrical extensions on inflow and outflow segments [29]. The CB models were clipped at CCA3, ICA5, and ECA5 borders [26] for global comparison of the wall area hemodynamic parameters.

D. Computational Simulations

Our pilot work [27] on the influence of various head postures and varying degree of head rotation on both the geometric and hemodynamic characteristics of the CB suggested that only significant geometric changes can influence the hemodynamic properties in an emphatic and reproducible way. In this respect, two of the six volunteer model combinations (SPLC, SPRC, PPLC, PPRC for Vol. I and Vol. II) were selected for the computational simulations. Selection was based on the largest differences in CB geometry found between the supine and prone postures and specific criteria included: 1) bifurcation angle (Vol. I, SPRC versus PPRC: 41.9° versus 56.1°, Vol. II, SPRC versus PPRC: 30.5° versus 38.7°); 2) ICA angle (Vol. I, SPRC versus PPRC: 22.9° versus 35.6°, Vol. II, SPRC versus PPRC: 14.1° versus 14.6°); and 3) bifurcation area ratio (Vol. I, SPRC versus PPRC: 1.34 versus 1.92, Vol. II, SPRC versus PPRC: 1.0 versus 1.12). The S and P posture inlet waveforms were used for the corresponding left/right carotid model of each volunteer, but also for the model of the second postural position for that carotid. Therefore, a total of 16 computational simulations were performed, 8 for each of the two selected volunteers. The CFD simulations were based on various standard applied modeling assumptions, i.e., blood was considered Newtonian with a density of 1050 kg/m^3 and a viscosity of 3.5 cP, the artery wall rigid, and the inlet flow fully developed and laminar. The impact of these assumptions in computed hemodynamics has been discussed in [30]–[32].

1) Mesh Construction: The numerical solution of the governing equations of blood flow requires the spatial discretization of the computational domain. A systematic time step and grid size converge study has to be conducted for each patient-specific model [33] to ensure grid and time step convergence. Since, however, topology and flow features in all presented cases are expected to be roughly similar we conducted a grid and time step convergence study on a single case, and acquired results were applied to all cases. ICEM-CFD v12.1 (Ansys Inc.) was used to generate spatial discretizations of the computational domain with increasing mesh density (coarse, medium, fine) and three different time steps for the same carotid model (see Table I). Three monitor points were placed inside the carotid bulb, where the flow is characterized as complex. The results for the cycle averaged pressure (p) and velocity (u) at these points were calculated at the third flow cycle. The percentage differences between the computed p and u values became small (less than 11%) between medium to fine meshes and b and c time steps. The results for the monitor points investigated are summarized in Table I. Therefore a mesh size of $\sim 7.9 \times 10^5$ elements and a time step of 1.97×10^{-4} s were considered sufficient and were used in all models. A higher grid density (25% reduction in element size) was only applied in the vicinity of the CB and a refined viscous layer was added adjacent to the wall.

TABLE I
MESH CONSTRUCTION STUDY OF VELOCITY (m/s)/PRESSURE (mmHg) AT PEAK SYSTOLE FOR THE THREE MONITOR POINTS (MP) PLACED IN CAROTID BULB

			Time Step ($\cdot 10^{-4}$ s)		
		MP	3.95	1.97	1.32
Grid Size ($\cdot 10^5$ elements)	~4.8	1	0.35/3.03	0.11/2.27	0.38/2.08
		2	0.45/2.87	0.47/2.09	0.48/1.90
		3	0.11/3.09	0.11/2.32	0.11/2.13
	~7.9	1	0.34/3.18	0.36/2.41	0.37/2.10
		2	0.45/3.00	0.47/2.24	0.48/1.93
		3	0.11/3.27	0.11/2.47	0.11/2.17
	~19	1	0.42/0.69	0.42/0.69	0.45/0.68
		2	0.53/0.82	0.53/0.81	0.54/0.81
		3	0.10/0.82	0.10/0.81	0.09/0.80

2) Flow Waveforms: The blood flow time history obtained with PC-MRI by integrating the through-plane velocity over the lumen cross-sectional area at every frame using Segment v1.9 R2178 [34]. The data were decomposed in 14 harmonics with fast Fourier transform using MatlabR2012b (The MathWorks Inc.). The resulting waveforms were used to compute the fully developed inlet time-varying velocity profiles for each case. Regarding outlet boundary conditions, a fixed flow division of 65/35 between ECA/ICA [35] and traction-free conditions were applied.

3) Data Analysis: To compare blood flow rates (Q) at the same heart rate (HR), all flow rates were scaled to a constant heart rate of 60 beats per minute:

$$Q_{\text{scaled}} = Q_{\text{measured}} \left(\frac{60}{HR_{\text{measured}}} \right) \tag{1}$$

Statistical analysis was performed using the R language v3.0.2 (the R project for statistical computing) and data are presented as mean $\pm$ standard deviation (s.d.). The Wilcoxon signed-rank test was used for comparisons between supine and prone head postures. The value $p < 0.05$ was considered to indicate significance.

4) Flow Computations: Fluent v12.1 (Ansys Inc.) was used to obtain numerical solutions. Actual recorded heart rates were used in each case to obtain simulation time step for 4000 iterations per cycle. The Womersley number (α, based on inlet radius) was $4.72 \leq \alpha \leq 5.35$. A second-order upwind scheme was applied for the discretization of the momentum equations and a second-order interpolation scheme for pressure. The Pressure-Implicit with Splitting of Operators (PISO) algorithm was used for pressure-velocity coupling. A time periodic solution was achieved after three flow cycles. Data of the fourth and fifth cycle were used. Hemodynamic parameters, such as time-averaged WSS (TAWSS), OSI, nOSI, RRT, helicity (HL), were computed. OSI was first defined by Ku *et al.* [12] and was later modified by Papaharilaou *et al.* as follows [36]:

$$\text{OSI} = \frac{\int_0^T w \left| \tau_w \cdot n_m \right| dt}{\int_0^T \left| \tau_w \cdot n_m \right| dt}, \qquad 0 \leq \text{OSI} \leq 1/2 \tag{2}$$

$$n_m = \frac{1}{T} \int_0^T \left(\frac{\tau}{\|\tau\|} \right) dt \tag{3}$$

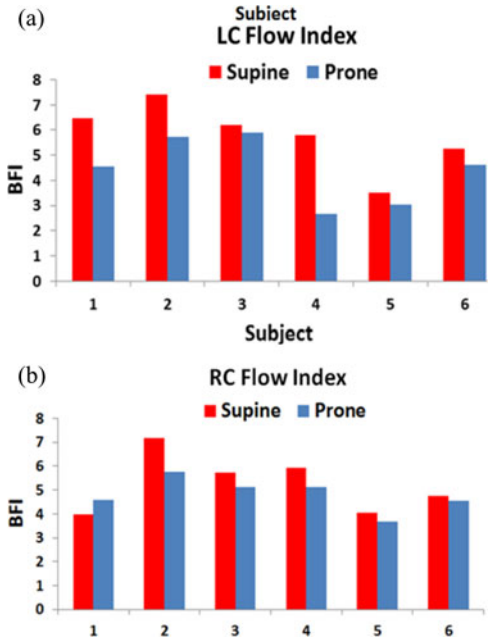

Fig. 1. Blood flow index (BFI) through the (a) left and (b) right CCA for each volunteer and for both head postures.

where T is the heart cycle period, $\boldsymbol{\tau}$ is the instantaneous WSS vector, n_m is the mean shear direction, and w is defined according to:

$$w = 0.5(1 - \cos \alpha) \tag{4}$$

where α is the angle between $\boldsymbol{\tau}$ and n_m. An OSI value of 0 corresponds to unidirectional shear flow, while 0.5 corresponds to a purely oscillatory shear. nOSI is calculated by dividing OSI with the TAWSS magnitude normalized by the time-averaged inlet Poiseuille flow. RRT was proposed by Himburg *et al.* [37] and is defined as:

$$\text{RRT} = \frac{1}{(1 - 2 \cdot \text{OSI}) \times \text{WSS}_{\text{Poiseuille}}} \tag{5}$$

where $\text{WSS}_{\text{Poiseuille}}$ is the Poiseulle flow WSS at the inlet.

HL(t) was introduced by Moffat and Tsinober [38] and for a fluid in a domain D is defined as

$$\text{HL}(t) = \int_D v(x,t) \cdot \nabla \times v(x,t) dV = \int_D v(x,t) \cdot \omega(x,t) dV. \tag{6}$$

Finally, the localized normalized helicity (LNH) used in this study is defined in [39] as

$$\text{LNH}(x,t) = \frac{v(x,t) \cdot \omega(x,t)}{|v(x,t)| \, |\omega(x,t)|}, \qquad -1 \leq \text{LNH} \leq 1. \tag{7}$$

Positive values of helicity are related to clockwise blood rotation and negative ones to counterclockwise blood rotation.

III. RESULTS

The inlet blood flow histograms at CCA change with head posture as illustrated in Fig. 1. Fig. 1(a) and (b) show the blood flow index (BFI) for the six volunteers in the supine and prone position for the left and the right carotid, respectively. The BFI

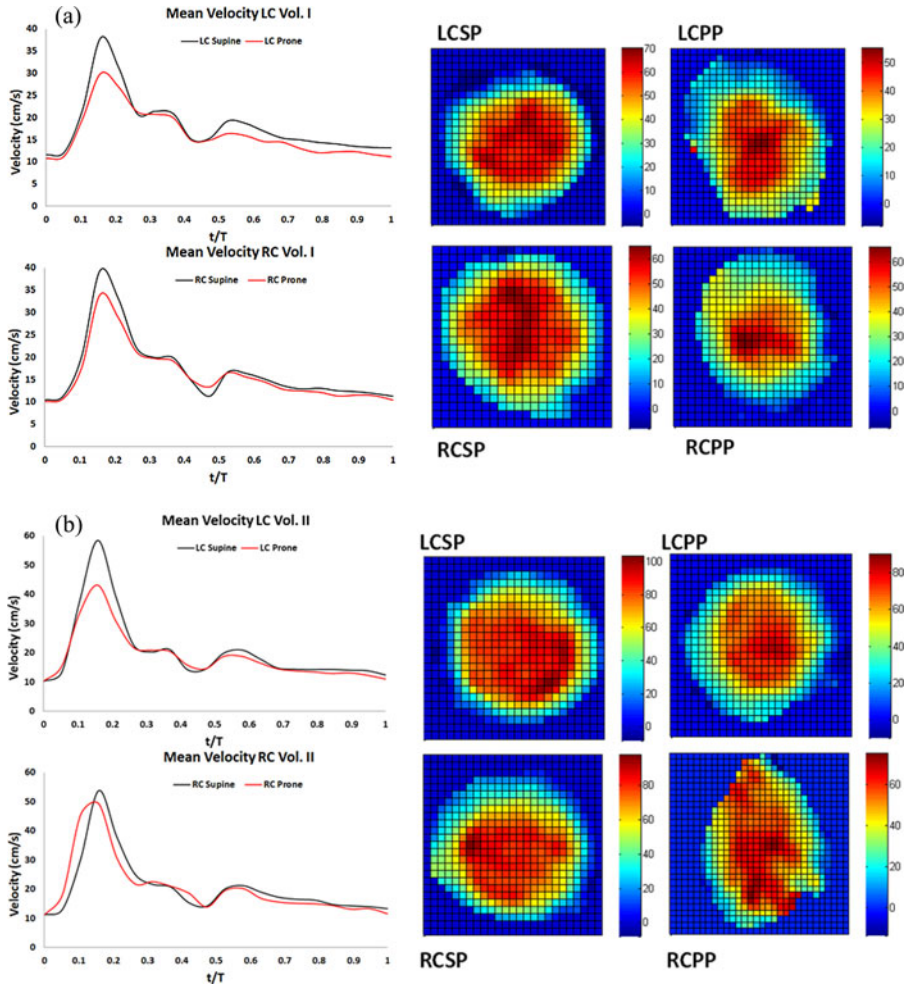

Fig. 2. Inlet velocity waveforms (left) and lumen cross-sectional velocity distribution at peak systole (right) for (a) volunteer I and (b) volunteer II.

in this study is defined by

$$\mathrm{BFI} = \frac{Q_{\mathrm{sys}}}{Q_{\mathrm{dia}}} \tag{8}$$

where Q_{sys} is the blood flow at peak systole and $\mathrm{Q_{dia}}$ the flow at end diastole. It is evident that prone position is associated with reduced BFI in most cases.

Fig. 2 represents the velocity waveforms used as inlet boundary conditions for volunteer I (a) and volunteer II (b). For each case, the cross-sectional distribution of peak systolic velocities is also shown. As observed, head rotation does not affect significantly the flow waveform but it reduces the peak systolic blood velocity.

Table II lists the measured and scaled CCA flow rate (mean $\pm$ s.d.) from all six volunteers. The results indicate a notable decrease of peak blood flow rate for the prone posture.

Fig. 3 shows the computed isosurfaces of LNH averaged over the cardiac cycle (top) and the corresponding isosurfaces at peak systole (middle) and end diastole (bottom). The isosurfaces of LNH averaged over the cardiac cycle indicate a region of high intensity helicity, where bidirectional helical structures are represented by blue (clockwise) and red (counterclockwise) tracts. These flow structures originate at the bifurcation region and develop into the ICA and ECA. These patterns were conserved for both head postures in the left CB, but have shown variation in the LNH direction and spatial extent in the right CB. The comparison of the instantaneous LNH at peak systole and end diastole shows differences in direction and spatial extent for almost all cases demonstrating that geometric changes combined with dynamic changes in the pressure distribution cause instantaneous changes in the helical structure distribution.

TABLE II
MEAN VALUES AND STANDARD DEVIATIONS OF THE PEAK BLOOD FLOW RATE (Q, MEASURED AND SCALED) FOR THE SUPINE (S) AND THE PRONE (P) WITH RIGHTWARD ROTATION POSTURES FOR BOTH CCAS

Artery (n=12)	Head Posture	Measured $\mathrm{Q_{peak}}$ ($\mathrm{cm^3/sec}$)	p	Scaled $\mathrm{Q_{peak}}$ ($\mathrm{cm^3/sec}$)	p
BOTH CCAs	S	19.10±3.90	0.02*	17.48±3.54	0.002*
	P	17.00±3.96		14.73±3.19	

*Denotes statistically significant difference ($p < 0.05$) in Wilcoxon signed-rank test between the two investigated head postures.

Figs. 4 and 5 show the head posture related changes in the exposure of the carotid wall to unfavorable hemodynamics. In more detail, Fig. 4 shows contour plots of nOSI and the contour line for the threshold value of nOSI $= 1.125$ to visualize the atherosclerosis susceptibility areas (nOSI$>$1.125).

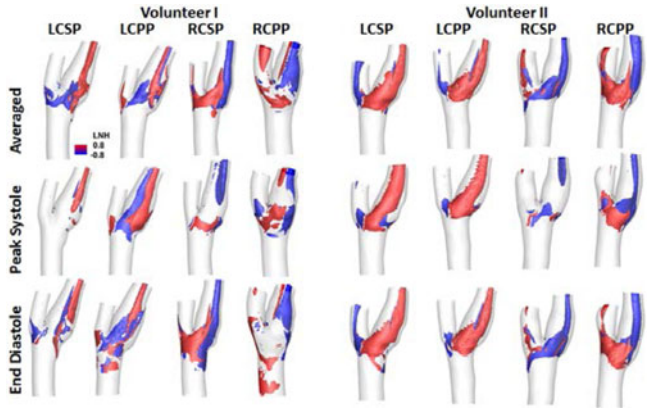

Fig. 3. Localized normalized helicity (LNH) isosurfaces for the two investigated head postures: averaged throughout the cardiac cycle (top), instantaneous at peak systole (middle) and instantaneous at end diastole. LNH = 0.8 indicates clockwise blood rotation and LNH = –0.8 counterclockwise rotation.

To investigate the effects of geometry and inlet flow waveform on the computed flow field, the contour plots are presented for the corresponding inlet flow waveforms of each position as well as for the alternative waveform, i.e., supine geometry-supine inlet waveform, prone geometry-prone inlet waveform, supine geometry-prone inlet waveform, prone geometry-supine inlet waveform. This way, we attempt to distinguish and compare the sensitivity of the flow field on both the geometry and inlet flow waveform. Similarly, Fig. 5 shows the distribution of RRT. The comparison of nOSI and RRT fields in Figs. 4 and 5, respectively, depicts the discernible influence that posture-related geometry and inlet flow waveform changes pose on these parameters.

The quantification of the impact of unfavorable hemodynamics on the arterial wall is presented in Table III. The definition of unfavorable hemodynamics is based on threshold values. For TAWSS the threshold adopted was 0.4 Pa as indicated by Malek *et al.* [13]. For high values of OSI we selected three thresholds (0.145, 0.238 and 0.3). The first two values were proposed by Lee *at al.* [40], while the third one was selected arbitrarily to assess the sensitivity of our results. The nOSI threshold adopted (1.125) was calculated based on the respective thresholds for OSI and TAWSS and by normalizing TAWSS with the average value of WSS in arteries of 1.5 Pa from the data of Malek *et al.* [13]. The selected RRT thresholds (9.35, 5.29, 7.14) were calculated from (4) and the corresponding OSI thresholds. Presented data, manifest the role that inlet waveform plays in highlighting the area exposed to unfavorable conditions. When a nonmatching waveform is used, differences due to head posture change are mitigated.

IV. Discussion

This study, focused on the changes in the CCA flow and important CB hemodynamic parameters caused by head and neck rotation using patient-specific geometries and inlet velocity waveforms. The new information presented here, as demonstrated by Figs. 1 and 2, is the notable decrease in blood flow rate at peak systole with rightward head rotation. For the left CB, BFI was reduced in all cases, while a similar reduction was seen for the right CB in 5 out of 6 volunteers (see Fig. 1). This may be due to changes in the local resistance or downstream impedance with head rotation that could cause reduction of peak systolic blood flow and it may also be related to slight alterations in the heart rate of volunteers between the two scanning sessions. In addition, rightward head rotation seems to slightly increase total CCA flow at end diastole, which in combination with the reduced peak systolic flow results in the observed BFI changes. Nevertheless, the shape of the flow waveform remains unaffected as indicated in Fig. 2, which also indicates that head posture affects the cross sectional distribution of peak systolic velocities. Rightward rotation seems to extenuate the occurrence of high velocities at the periphery of the lumen and accentuate the velocity distribution skewness. Interestingly enough, CCA flow velocity, as well as CCA diameter, seem to be associated with ischemic stroke independently of carotid atherosclerosis and CVD risk factors [41].

For two volunteers that have shown significant geometric alterations due to head rotation, we combined the CCA blood flow waveforms measured for both head postures with CB-specific geometries to independently compute relevant blood flow fields. Significant hemodynamic changes were observed.

The general features of the flow field in terms of the localized normalized helicity (LNH) are illustrated in Fig. 3 where the isosurfaces of LNH are shown. We applied a threshold of 0.8 to highlight high helicity regions [39]. Overall, LNH revealed a strong subject and vessel dependency. Head rotation does not seem to favor clockwise or counterclockwise blood rotation, although it significantly affects the instantaneous spatial extent of the LNH. As outlined by Gallo *et al.* [39], helicity of high intensity may suppress flow disturbances and, thus, prevent plaque deposition [42].

The comparison of the flow field dependency on geometry and inlet flow waveform shows that when the geometry is kept constant and the inlet waveform changes (horizontal comparison in Figs. 4 and 5), the pattern of the atherosclerosis susceptible wall regions is very similar, although nOSI in particular, also shows quantitative differences. This is in agreement with the results of Campell *et al.* [43], who investigated the effect of inlet waveform on CFD simulations using blunt, parabolic, Womersley or the real subject profile, and those of Moyle *et al.* [30] who found that geometric parameters influence the hemodynamic features more significantly than the inlet waveform. Indeed, when the inlet waveform is kept constant and the geometric model is altered due to postural changes (diagonal comparison), the atherosclerosis susceptible wall regions alter both qualitatively and quantitatively. However, when the realistic conditions are taken into account (vertical comparison between the first pair in each category), it appears that the rotation-derived changes in the "sensitive" carotid wall regions are extenuated. This may indicate that the interrelation between geometry and flow waveform tends to autoregulate disturbed flow fields and moderate unfavorable conditions. These suggestions are quantitatively supported by data presented in Table III. As highlighted by the difference in corresponding calculated wall regions between the two head postures (grayed rows), the adoption of a common inlet flow waveform can significantly differentiate the

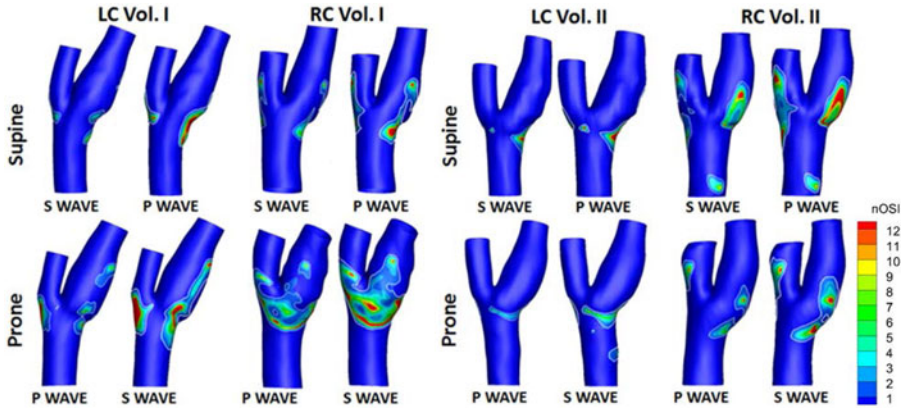

Fig. 4. Contour plots of nOSI for the left (LC) and right carotid (RC) for volunteers I and II. The first row represents the supine normal head position and the second row the prone position with rightward head rotation. S WAVE corresponds to CFD results obtained using the inlet waveform obtained from the supine position, while P WAVE corresponds to CFD results using the prone position waveform. nOSI = 1.125 is shown as a white contour line.

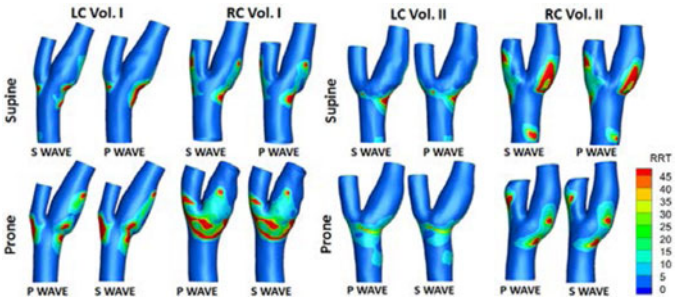

Fig. 5. Contour plots of RRT for the left (LC) and right carotid (RC) for volunteers I and II. The first row represents the supine normal head position and the second row the prone position with rightwards head rotation. S WAVE corresponds to CFD results obtained from the supine position, while P WAVE corresponds to CFD results using the prone position waveform.

TABLE III
AREA EXPOSED TO UNFAVORABLE HEMODYNAMICS NORMALIZED BY THE TOTAL SURFACE AREA BOUNDED BY CCA3, ECA5, AND ICA5 FOR THE TWO HEAD POSTURES

		Volunteer I				Volunteer II			
		LC		RC		LC		RC	
		Phys.	Alt.	Phys.	Alt.	Phys.	Alt.	Phys.	Alt.
TAWSS < 0.32 (Pa)	S	0.28	0.37	0.37	0.32	0.16	0.23	0.22	0.21
	P-S	0.11	-0.06	-0.14	-0.09	0.08	0.05	0	-0.02
TAWSS < 0.4 (Pa)	S	0.36	0.45	0.46	0.4	0.21	0.26	0.26	0.27
	P-S	0.16	-0.06	-0.19	-0.12	0.09	0.08	-0.06	-0.05
TAWSS < 0.48 (Pa)	S	0.43	0.54	0.52	0.48	0.27	0.3	0.31	0.33
	P-S	0.14	-0.06	-0.21	-0.15	0.08	0.09	-0.05	-0.09
OSI > 0.3	S	0.04	0.04	0.05	0.02	0.09	0.06	0.04	0.05
	P-S	-0.03	-0.01	-0.03	0	0.01	0.02	0.02	0.01
OSI > 0.145	S	0.12	0.11	0.19	0.13	0.33	0.15	0.15	0.16
	P-S	-0.03	0.02	-0.09	0	-0.08	0.07	0.05	0.03
OSI > 0.238	S	0.07	0.06	0.1	0.05	0.16	0.09	0.08	0.09
	P-S	-0.03	0	-0.06	0	-0.01	0.03	0.04	0.02
nOSI > 1.125	S	0.1	0.15	0.12	0.02	0.06	0.15	0.19	0.13
	P-S	0	0	-0.05	0.11	0.04	0.03	-0.09	0.03
RRT > 9.35	S	0.14	0.16	0.18	0.14	0.11	0.13	0.11	0.1
	P-S	0.01	-0.03	-0.07	-0.03	0.04	0.02	0.02	0.03
RRT > 5.29	S	0.21	0.24	0.28	0.23	0.18	0.19	0.17	0.17
	P-S	0.04	-0.03	-0.11	-0.06	0.04	0.03	0.01	0.01
RRT > 7.14	S	0.17	0.2	0.22	0.18	0.14	0.16	0.14	0.13
	P-S	0.02	-0.03	-0.09	-0.05	0.04	0.02	0.02	0.02

Phys. : Physiological waveform e.g. supine position - supine waveform, prone position - prone waveform.
Alt. : Alternative waveform e.g. supine position – prone waveform, prone position – supine waveform.

carotid wall region potentially prone to plaque development. It is proposed, therefore, to use a posture-specific inlet waveform in CFD simulations related to postural effects.

However, caution should be exercised in the interpretation of the results of our study due to the small number of subjects used. A large cohort is needed to ensure that the changes observed are statistically significant to disambiguate definite trends in specific geometric and hemodynamic parameters with posture change. Inaccuracies in the identification of the arterial wall and arterial lumen in each segment due to low signal to noise ratio and flow voids has been a problem in this study and its importance has been highlighted before [27], [28]. The rigid wall assumption considered in this study is also a limitation. Nevertheless, the findings of this study can be considered as complementary to work presented in references 32 and 33 in associating a patient specific CB geometry with disturbance indices and increased risk of disease development.

V. CONCLUSION

Head rotation inflicts changes on the geometric characteristics of the CB, as well as on the CCA blood flow waveform. These changes affect the developed flow fields and influence the exposure of the carotid wall to unfavorable hemodynamics. The prominent intersubject variability of these changes warrant an individualized approach for the evaluation of the potential risks that head posture may pose on plaque deposition and/or rupture of existent vulnerable lesions as well as on potential fractures of stents in stented vessels.

REFERENCES

[1] A. S. Go, D. Mozaffarian, V. L. Roger, E. J. Benjamin, J. D. Berry, W. B. Borden, D. M. Bravata, S. Dai, E. S. Ford, C. S. Fox, S. Franco, H. J. Fullerton, C. Gillespie, S. M. Hailpern, J. A. Heit, V. J. Howard, M. D. Huffman, B. M. Kissela, S. J. Kittner, D. T. Lackland, J. H. Lichtman, L. D. Lisabeth, D. Magid, G. M. Marcus, A. Marelli, D. B. Matchar, D. K. McGuire, E. R. Mohler, C. S. Moy, M. E. Mussolino, G. Nichol, N. P. Paynter, P. J. Schreiner, P. D. Sorlie, J. Stein, T. N. Turan, S. S. Virani, N. D. Wong, D. Woo, M. B. Turner, C. American Heart Association Statistics, and S. Stroke Statistics, "Executive summary: Heart disease and stroke statistics—2013 update: A report from the American Heart Association," *Circulation*, vol. 127, pp. 143–52, Jan. 1, 2013.

[2] M. Nichols, N. Townsend, P. Scarborough, R. Luengo-Fernandez, J. Leal, A. Gray, and M. Rayner, "European cardiovascular disease statistics 2012," in *European Heart Network*. Brussels, Belgium: European Society of Cardiology, Sophia Antipolis, 2012.
[3] D. T. Miller, P. M. Ridker, P. Libby, and D. J. Kwiatkowski, "Atherosclerosis: The path from genomics to therapeutics," *J. Amer. Coll. Cardiol.*, vol. 49, pp. 1589–1599, Apr. 17, 2007.
[4] D. N. Ku, "Blood flow in arteries," *Annu. Rev. Fluid Mech.*, vol. 29, pp. 399–434, 1997.
[5] O. Araim, A. Chen, and B. Sumpio, "Hemodynamic forces effects on atherosclerosis," *Eurekah Biosci.*, vol. 1, pp. 39–46, 2005.
[6] S. Z. Zhao, X. Y. Xu, A. D. Hughes, S. A. Thom, A. V. Stanton, B. Ariff, and Q. Long, "Blood flow and vessel mechanics in a physiologically realistic model of a human carotid arterial bifurcation," *J. Biomech.*, vol. 33, pp. 975–984, 2000.
[7] A. S. Anayiotos, S. A. Jones, D. P. Giddens, S. Glagov, and C. K. Zarins, "Shear-stress at a compliant model of the human carotid bifurcation," *J. Biomech. Eng. Trans. ASME*, vol. 116, pp. 98–106, Feb. 1994.
[8] D. Martin, A. Zaman, J. Hacker, D. Mendelow, and D. Birchall, "Analysis of haemodynamic factors involved in carotid atherosclerosis using computational fluid dynamics," *Brit. J. Radiol.*, vol. 82, no. 1, pp. S33–S38, Jan. 2009.
[9] R. Ross, "Atherosclerosis is an inflammatory disease," *Amer. Heart J.*, vol. 138, pp. S419–S420, Nov. 1999.
[10] K. Perktold and G. Rappitsch, "Computer simulation of local blood flow and vessel mechanics in a compliant carotid artery bifurcation model," *J. Biomech.*, vol. 28, pp. 845–856, Jul. 1995.
[11] S. W. Lee, L. Antiga, and D. A. Steinman, "Correlations among indicators of disturbed flow at the normal carotid bifurcation," *J. Biomech. Eng.*, vol. 131, p. 061013, Jun. 2009.
[12] D. N. Ku, D. P. Giddens, C. K. Zarins, and S. Glagov, "Pulsatile flow and atherosclerosis in the human carotid bifurcation—Positive correlation between plaque location and low and oscillating shear-stress," *Arteriosclerosis*, vol. 5, pp. 293–302, 1985.
[13] A. M. Malek, S. L. Alper, and S. Izumo, "Hemodynamic shear stress and its role in atherosclerosis," *JAMA*, vol. 282, pp. 2035–2042, Dec. 1, 1999.
[14] D. A. Steinman and C. A. Taylor, "Flow imaging and computing: Large artery hemodynamics," *Ann. Biomed. Eng.*, vol. 33, pp. 1704–1709, Dec. 2005.
[15] C. A. Taylor and D. A. Steinman, "Image-based modeling of blood flow and vessel wall dynamics: Applications, methods and future directions: Sixth International Bio-Fluid Mechanics Symposium and Workshop, March 28–30, 2008 Pasadena, California," *Ann. Biomed. Eng.*, vol. 38, pp. 1188–1203, Mar. 2010.
[16] L. Antiga, M. Piccinelli, L. Botti, B. Ene-Iordache, A. Remuzzi, and D. A. Steinman, "An image-based modeling framework for patient-specific computational hemodynamics," *Med. Biol. Eng. Comput.*, vol. 46, pp. 1097–1112, Nov. 2008.
[17] Q. Long, X. Y. Xu, B. Ariff, S. A. Thom, A. D. Hughes, and A. V. Stanton, "Reconstruction of blood flow patterns in a human carotid bifurcation: A combined CFD and MRI study," *J. Magn. Reson. Imag.*, vol. 11, pp. 299–311, Mar. 2000.
[18] D. A. Steinman, J. B. Thomas, H. M. Ladak, J. S. Milner, B. K. Rutt, and J. D. Spence, "Reconstruction of carotid bifurcation hemodynamics and wall thickness using computational fluid dynamics and MRI," *Magn. Reson. Med.*, vol. 47, pp. 149–159, Jan. 2002.
[19] M. R. Kaazempur-Mofrad, M. Bathe, H. Karcher, H. F. Younis, H. C. Seong, E. B. Shim, R. C. Chan, D. P. Hinton, A. G. Isasi, A. Upadhyaya, M. J. Powers, L. G. Griffith, and R. D. Kamm, "Role of simulation in understanding biological systems," *Comput. Struct.*, vol. 81, pp. 715–726, 2003.
[20] P. B. Bijari, L. Antiga, B. A. Wasserman, and D. A. Steinman, "Scan-rescan reproducibility of carotid bifurcation geometry from routine contrast-enhanced MR angiography," *J. Magn. Reson. Imag.*, vol. 33, pp. 482–489, Feb. 2011.
[21] J. B. Thomas, J. S. Milner, B. K. Rutt, and D. A. Steinman, "Reproducibility of image-based computational fluid dynamics models of the human carotid bifurcation," *Ann. Biomed. Eng.*, vol. 31, pp. 132–141, 2003.
[22] I. Marshall, S. Zhao, P. Papathanasopoulou, P. Hoskins, and Y. Xu, "MRI and CFD studies of pulsatile flow in healthy and stenosed carotid bifurcation models," *J. Biomech.*, vol. 37, pp. 679–687, May 2004.
[23] J. R. Cebral, P. J. Yim, R. Löhner, O. Soto, and P. L. Choyke, "Blood flow modeling in carotid arteries with computational fluid dynamics and MR imaging," *Academic Radiol.*, vol. 9, pp. 1286–1299, 2002.
[24] L. Goubergrits, U. Kertzscher, B. Schoneberg, E. Wellnhofer, C. Petz, and H. C. Hege, "CFD analysis in an anatomically realistic coronary artery model based on non-invasive 3D imaging: Comparison of magnetic resonance imaging with computed tomography," *Int. J. Cardiovasc Imag.*, vol. 24, pp. 411–421, Apr. 2008.
[25] J. A. Moore, D. A. Steinman, D. W. Holdsworth, and C. R. Ethier, "Accuracy of computational hemodynamics in complex arterial eometries reconstructed from magnetic resonance imaging," *Ann. Biomed. Eng.*, vol. 27, pp. 32–41, Jan.-Feb. 1999.
[26] N. Aristokleous, I. Seimenis, Y. Papaharilaou, G. C. Georgiou, B. C. Brott, E. Eracleous, and A. S. Anayiotos, "Effect of posture change on the geometric features of the healthy carotid bifurcation," *IEEE Trans Inf. Technol. Biomed.*, vol. 15, no. 1, pp. 148–154, Jan. 2011.
[27] Y. Papaharilaou, N. Aristokleous, I. Seimenis, M. I. Khozeymeh, G. C. Georgiou, B. C. Brott, E. Eracleous, and A. S. Anayiotos, "Effect of head posture on the healthy human carotid bifurcation hemodynamics," *Med. Biol. Eng. Comput.*, vol. 51, pp. 207–218, Feb. 2013.
[28] P. A. Yushkevich, J. Piven, H. C. Hazlett, R. G. Smith, S. Ho, J. C. Gee, and G. Gerig, "User-guided 3D active contour segmentation of anatomical structures: Significantly improved efficiency and reliability," *Neuroimage*, vol. 31, pp. 1116–1128, Jul. 1, 2006.
[29] L. Antiga and D. A. Steimman, "Robust and objective decompositionand mapping of bifurcating vessels," *IEEE Trans. Med. Imag.*, vol. 23, no. 6, pp. 704–713, Jun. 2004.
[30] K. R. Moyle, L. Antiga, and D. A. Steinman, "Inlet conditions for image-based CFD models of the carotid bifurcation: Is it reasonable to assume fully developed flow?," *J. Biomech. Eng.*, vol. 128, pp. 371–179, Jun. 2006.
[31] U. Morbiducci, D. Gallo, D. Massai, R. Ponzini, M. A. Deriu, L. Antiga, A. Redaelli, and F. M. Montevecchi, "On the importance of blood rheology for bulk flow in hemodynamic models of the carotid bifurcation," *J. Biomech.*, vol. 44, pp. 2427–2438, Sep. 2, 2011.
[32] U. Morbiducci, D. Gallo, D. Massai, F. Consolo, R. Ponzini, L. Antiga, C. Bignardi, M. A. Deriu, and A. Redaelli, "Outflow conditions for image-based hemodynamic models of the carotid bifurcation: Implications for indicators of abnormal flow," *J. Biomech. Eng.*, vol. 132, p. 091005, Sep. 2010.
[33] S. Hodis, S. Uthamaraj, A. L. Smith, K. D. Dennis, D. F. Kallmes, and D. Dragomir-Daescu, "Grid convergence errors in hemodynamic solution of patient-specific cerebral aneurysms," *J. Biomech.*, vol. 45, pp. 2907–2913, Nov. 15, 2012.
[34] E. Heiberg, J. Sjogren, M. Ugander, M. Carlsson, H. Engblom, and H. Arheden, "Design and validation of segment–freely available software for cardiovascular image analysis," *BMC Med. Imag.*, vol. 10, p. 1, 2010.
[35] H. C. Groen, L. Simons, Q. J. van den Bouwhuijsen, E. M. Bosboom, F. J. Gijsen, A. G. van der Giessen, F. N. van de Vosse, A. Hofman, A. F. van der Steen, J. C. Witteman, A. van der Lugt, and J. J. Wentzel, "MRI-based quantification of outflow boundary conditions for computational fluid dynamics of stenosed human carotid arteries," *J. Biomech.*, vol. 43, pp. 2332–2338, Aug. 26, 2010.
[36] Y. Papaharilaou, D. J. Doorly, and S. J. Sherwin, "The influence of out-of-plane geometry on pulsatile flow within a distal end-to-side anastomosis," *J. Biomech.*, vol. 35, pp. 1225–1239, Sep. 2002.
[37] H. A. Himburg, D. M. Grzybowski, A. L. Hazel, J. A. LaMack, X. M. Li, and M. H. Friedman, "Spatial comparison between wall shear stress measures and porcine arterial endothelial permeability," *Amer. J. Physiol. Heart Circ. Physiol.*, vol. 286, pp. H1916–H1922, May 2004.
[38] H. K. Moffatt and A. Tsinober, "Helicity in laminar and turbulent-flow," *Annu. Rev. Fluid Mechanics*, vol. 24, pp. 281–312, 1992.
[39] D. Gallo, D. A. Steinman, P. B. Bijari, and U. Morbiducci, "Helical flow in carotid bifurcation as surrogate marker of exposure to disturbed shear," *J. Biomech.*, vol. 45, pp. 2398–2404, Sep. 21, 2012.
[40] S. W. Lee, L. Antiga, J. D. Spence, and D. A. Steinman, "Geometry of the carotid bifurcation predicts its exposure to disturbed flow," *Stroke*, vol. 39, pp. 2341–2347, Aug. 2008.
[41] C. H. Bai, J. R. Chen, H. C. Chiu, and W. H. Pan, "Lower blood flow velocity, higher resistance index, and larger diameter of extracranial carotid arteries are associated with ischemic stroke independently of carotid atherosclerosis and cardiovascular risk factors," *J. Clin. Ultrasound*, vol. 35, pp. 322–330, Jul.–Aug. 2007.
[42] U. Morbiducci, R. Ponzini, M. Grigioni, and A. Redaelli, "Helical flow as fluid dynamic signature for atherogenesis risk in aortocoronary bypass. A numeric study," *J. Biomech.*, vol. 40, pp. 519–534, 2007.
[43] I. C. Campbell, J. Ries, S. S. Dhawan, A. A. Quyyumi, W. R. Taylor, and J. N. Oshinski, "Effect of inlet velocity profiles on patient-specific computational fluid dynamics simulations of the carotid bifurcation," *J. Biomech. Eng.*, vol. 134, p. 051001, May 2012.

Authors' photographs and biographies not available at the time of publication.